Research Article | Vol. 11, No. 3 / 1 March 2020 / Biomedical Optics Express 1477
Biomedical Optics EXPRESS

Toward whole-brain *in vivo* optoacoustic angiography of rodents: modeling and experimental observations

PAVEL SUBOCHEV,[1,*] EKATERINA SMOLINA,[1] EKATERINA SERGEEVA,[1] MIKHAIL KIRILLIN,[1] ANNA ORLOVA,[1] DARIA KURAKINA,[1] DANIIL EMYANOV,[1] AND DANIEL RAZANSKY[2,3,4]

[1]*Institute of Applied Physics RAS, 46 Ulyanov Street, Nizhniy Novgorod, Russia*
[2]*Faculty of Medicine and Institute of Pharmacology and Toxicology, University of Zurich, Switzerland*
[3]*Institute for Biomedical Engineering and Department of Information Technology and Electrical Engineering, ETH Zurich, Switzerland*
[4]*Institute for Biological and Medical Imaging, Helmholtz Center Munich, Neuherberg, Germany*
[*]*Pavel.Subochev@gmail.com*

Abstract: Cerebrovascular imaging of rodents is one of the trending applications of optoacoustics aimed at studying brain activity and pathology. Imaging of deep brain structures is often hindered by sub-optimal arrangement of the light delivery and acoustic detection systems. In our work we revisit the physics behind opto-acoustic signal generation for theoretical evaluation of optimal laser wavelengths to perform cerebrovascular optoacoustic angiography of rodents beyond the penetration barriers imposed by light diffusion in highly scattering and absorbing brain tissues. A comprehensive model based on diffusion approximation was developed to simulate optoacoustic signal generation using optical and acoustic parameters closely mimicking a typical murine brain. The model revealed three characteristic wavelength ranges in the visible and near-infrared spectra optimally suited for imaging cerebral vasculature of different size and depth. The theoretical conclusions are confirmed by numerical simulations while in vivo imaging experiments further validated the ability to accurately resolve brain vasculature at depths ranging between 0.7 and 7 mm.

1. Introduction

Optoacoustic (OA) imaging is a hybrid technology based on wideband detection of ultrasonic waves generated due to absorption of laser pulses in optically heterogeneous media [1]. Hemoglobin is the major bio-chrome allowing for high-contrast OA angiography with optical contrast and ultrasonic spatial resolution. The high potential of OA angiography was confirmed in a number of clinical trials involving skin [2] and breast [3] lesions as well as numerous studies on small animal models [4].

Cerebrovascular OA imaging of rodents is one of the highly promising applications of the method aimed at studying brain activity and pathologies [5]. The first OA sinograms of major cerebral blood vessels were obtained in mice in the beginning of 2000s [6]. Recent OA studies attained functional neuroangiography of pial microvasculature at up to 500 μm depth under the skull of a rodent [7,8]. However, high resolution whole-brain OA neuroangiography through an intact skull and scalp remained challenging due to the strong light attenuation by the brain as well as frequency-dependent acoustic reflections and dispersion effects introduced by the skull [9–12].

In this manuscript we revisit the physics behind opto-acoustic signal generation and experimentally test optimal conditions for high-contrast non-invasive whole-brain optoacoustic angiography of rodents.

#377670 https://doi.org/10.1364/BOE.377670
Journal © 2020 Received 12 Sep 2019; revised 15 Nov 2019; accepted 19 Dec 2019; published 20 Feb 2020

Biomedical Optics EXPRESS

2. Materials and methods

2.1. Optical and acoustical properties of mouse head

Optical scattering and absorption spectra of ex vivo dissected mouse brain were measured with a spectrophotometer Specord 250 plus (Analytik Jena, Germany) equipped with an integrating sphere for efficiently collecting light from a diffusive sample. Brain soft tissues obtained from 12 mice were homogenized and divided into three samples. Each sample was placed in a 1-mm thick cuvette, and measurements of diffuse transmittance and reflectance were conducted. The results of the absorption and he absorption (μ_a) and reduced scattering (μ_s') coefficients reconstruction by the inverse Monte Carlo technique [13] were averaged over all samples. Figure 1 presents averaged spectra of optical absorption and transport ($\mu t = \mu_a + \mu_s'$) coefficients for whole blood [14] and brain tissues in the wavelength spectral range of 500-1100 nm together with error bars). While the visible range of wavelengths (up to ~600 nm) exhibits the highest optical absorption by whole blood, the longer wavelengths in the 1000-1100 nm infrared range correspond to the weakest attenuation of the optical fluence by the brain tissues. Brain soft tissues are characterized by smaller absorption compared to whole blood though typical features of blood absorption spectrum can be distinguished in the brain absorption spectrum indicating that brain tissues contain certain amount of blood. Note that our measured optical properties of the *ex vivo* brain tissue (Fig. 1) are consistent with the previously reported values [15].

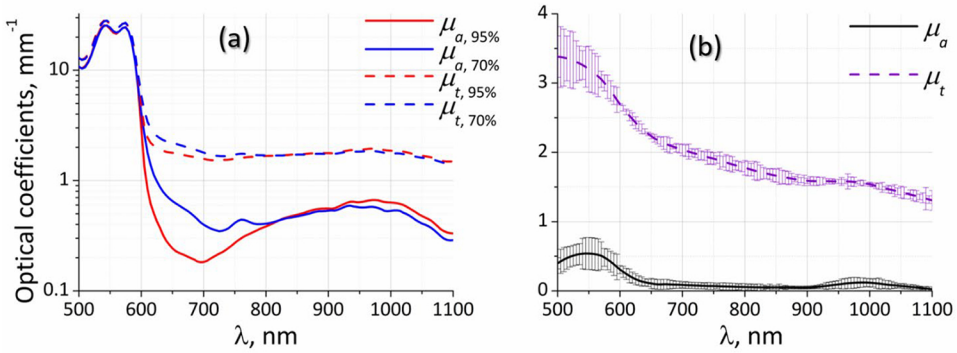

Fig. 1. Spectra of optical absorption (solid lines) and transport (dotted lines) coefficients of the mouse brain tissues *ex vivo*: (a) - whole blood with 95% oxygen saturation (red lines) and whole blood with 70% oxygen saturation (blue lines) [14]; (b) – dissected brain soft tissue.

Table 1 lists acoustic properties of a mouse head [16] representing their frequency-dependent attenuation properties governed by the exponential law $\sim \exp(-\alpha f^x z)$, where z is the propagation distance, f is acoustic frequency, α is ultrasonic attenuation constant, and x is frequency-dependence factor. Note that ultrasonic attenuation by skull has strong frequency dependence and is generally much stronger as compared to blood and brain tissues.

Table 1. Morphological and acoustical properties of the mouse brain, scalp and skull.

tissue type	thickness, mm	α, MHz^{-x}cm^{-1}	x
scalp	0.20	0.1	0.9
skull	0.35	1.2	2.1
brain	1-5	0.1	0.9
blood	0.1-0.5	0.1	0.9

Biomedical Optics EXPRESS

2.2. Theoretical model of OA signal formation in 1D

We consider a planar multi-layered model of the mouse head which contains layers representing scalp, skull, brain and an arbitrarily located blood layer mimicking the vessel cross-section (Fig. 2). Layers thicknesses of scalp, skull and upper layer of brain soft tissue are η, ξ and D, respectively; the vessel thickness is d, and the total thickness of the brain tissue covers the depth range between the planes $z = z_0$ and $z = z_3$. We subsequently solve the problem of pulsed transcranial optical illumination of the brain at the wavelength range $\lambda \in [500, 1100]$ nm followed by ultrawide-bandwidth ultrasonic detection of the generated OA signal.

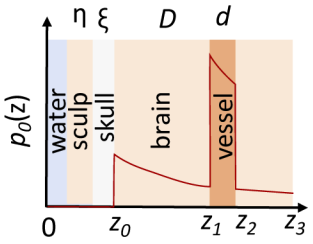

Fig. 2. Multi-layered model of the mouse head with a typical distribution of the absorbed optical energy density $p_0(z)$. Layers thicknesses are indicated as η (scalp), ξ (skull), D (upper brain soft tissue layer), d (vessel).

Using the diffusion approximation of the radiative transfer theory [17] for fluence calculation, we can estimate the depth-dependent distribution of initial OA pressure resulting from absorption of an infinitely short laser pulse as:

$$p_0(z) = \Gamma H_0 k_B [\Pi_{01} \mu_{a,B} e^{-\mu_B (z - z_0)} + \Pi_{12} \mu_a e^{-\mu (z - z_1) - \mu_B D} + \Pi_{23} \mu_{a,B} e^{-\mu_B (z - z_2) - \mu_B D - \mu d}], \quad (1)$$

where

$$k_B = 3 \frac{\mu_{t,\mathrm{B}}}{\mu_{\mathrm{B}}} \exp\left(-\frac{\mu_{\mathrm{B}}}{3\mu_{t,\mathrm{B}}}\right) \sinh\left(\frac{\mu_{\mathrm{B}}}{3\mu_{t,\mathrm{B}}}\right) \exp(-\langle \mu_{t,scalp} \rangle \eta) \exp(-\langle \mu_{t,s} \rangle \xi). \quad (2)$$

Here $p_0(z)$ is initial pressure distribution in the rodent head; Γ=0.5 is Grüneisen coefficient; H_0 is the incident fluence at the scalp surface $z = 0$ (chosen to be at $20\mathrm{mJ/cm^2}$ level in accordance with ANSI safety limits [18]); k_B is the scaling coefficient representing the normalized fluence at the brain upper surface $z = z_0$ after transmission through scalp and skull (detailed calculation is given in Appendix), $\mu = \sqrt{3\mu_a \mu_t}$ and $\mu_B = \sqrt{3\mu_{a,B}\mu_{t,B}}$ are effective attenuation coefficients of blood and brain, respectively; $\langle \mu_{t,s} \rangle$ and $\langle \mu_{t,scalp} \rangle$ are the transport coefficients of skull and scalp layers, respectively; μ_a and $\mu_{a,B}$ are optical absorption coefficients of blood and brain, respectively; $\mu_{\mathrm{t}} = \mu_a + \mu'$ and $\mu_{\mathrm{t,B}} = \mu_{a,B} + \mu'_B$ are transport coefficients of blood and brain; μ' and μ'_B are reduced optical scattering coefficients of blood and brain, respectively. The different tissue layers are analytically separated using boxcar step functions $\Pi_{\mathrm{ij}} = \theta(z - z_{\mathrm{i}})\theta(z_{\mathrm{j}} - z)$ expressed via Heaviside function $\theta(z)$.

All the optical coefficients of the brain and whole blood in Table 1 and Eqs. (1)–(2) are expressed via μ_a, $\mu_{a,B}$, μ_{t}, and $\mu_{\mathrm{t,B}}$ (Fig. 1), which are wavelength dependent according to Fig. 1, while scalp and skull transport coefficients are replaced by their average values in the 455-705 nm range, i.e. $\langle \mu_{t,s} \rangle = 2\,\mathrm{mm^{-1}}$ and $\langle \mu_{t,scalp} \rangle = 1\,\mathrm{mm^{-1}}$ according to the experimental data reported in [19] and [20].

Equation (2) is solution of the diffusion equation in the case of matched optical refractive indices at the water-tissue interface [21], an important practical case for OA imaging corresponding to matched acoustical impedances. If optical irradiation is performed through the air-tissue interface, total internal reflection plays a significant role, and the coefficient k_B should be estimated using proper boundary conditions [22] or the solutions based on the approximation of numerical results

Biomedical Optics EXPRESS

[23]. It should be noted that the applicability of diffusive approximation (1-2) is limited to relatively deeply-seated $D \gg 1/(\mu_{a,B} + \mu_{s,B})$ and thick $d \gg 1/(\mu_a + \mu_s)$ blood layers. Besides, the applicability of the proposed 1D model of OA signal formation is limited by the case of vessels located parallel to the skull boundary, and the vessel diameter is assumed to be large with respect to the typical transversal resolution of OA system.

To simulate frequency-dependent acoustic propagation toward the ultrasonic detector, a low-pass spatial filter determined by the thickness of brain and skull tissues with attenuation constants α_B and α_s and power law exponents x_B and x_s (Table 1) is applied to the initial pressure distribution (1):

$$\widetilde{p_0}(z) = \frac{1}{2}\sum_{n=-\infty}^{\infty} p_n \exp(-\alpha_B |f_n|^{x_B} D) \exp(-\alpha_s |f_n|^{x_s} \xi) e^{ik_n z}, \tag{3}$$

where $p_n = \frac{1}{z_3}\int_{-\frac{z_3}{2}}^{\frac{z_3}{2}} p_0(z) e^{-ik_n z} dz$, $k_n = n\frac{2\pi}{z_3}$, $f_n = n\frac{c_B}{z_3}$, $n \in Z$; $c_B = 1.5$ mm/μs is the sound speed in the brain tissue.

It should be noted, that Eq. (3) omits some effects of acoustic wave interaction with the skull. According to the experimental observations [24,25], skull insertion loss can be neglected when the skull thickness is smaller than the wavelength of acoustical wave interacting with it. Therefore, the reflections of acoustical wave by the surface of the typical adult rodent skull (~0.35 mm thick [16]) can be neglected in Eq. (3), when maximum frequency of ultrasonic detector f_n used for deep cerebrovascular OA imaging is limited by 10 MHz.

The integrated OA signal generated by the blood vessel and measured by a wideband ultrasonic detector with a given noise equivalent pressure (NEP) can be estimated via

$$P(\lambda, D, d) = \int_{z_1=z_{0+D}}^{z_2=z_0+D+d} |\widetilde{p_0}(z)\theta(\widetilde{p_0}(z) - NEP) - \widetilde{p_b}(z)\theta(\widetilde{p_b}(z) - NEP)| dz \tag{4}$$

where

$$p_b(z) = \Gamma H_0 k_B [\Pi_{03} \mu_{a,B} e^{-\mu_B (z - z_0)}] \tag{5}$$

is the initial pressure distribution in the uniform brain tissue and the distribution $\widetilde{p_b}(z)$ can be derived from $p_b(z)$ in accordance with Eq. (3).

Using methodology similar to [26], typical noise equivalent pressure of a disk-shaped PVDF detector (5 mm aperture, 5 μm PVDF film thickness) was measured with respect to RMS noise as NEP = 1.3 mPa/$\sqrt{\text{Hz}}$.

2.3. *In vivo* experiments and data processing

In vivo cerebral OA angiography of rodents was performed at the probing wavelengths of 532 nm and 1064 nm using raster-scan OA imaging setup schematically depicted in Fig. 3.

For this, a six-week-old balb-c mouse was anaesthetized with an intraperitoneal injection of the mixture of Zoletil 100 (20 mg/kg) with Rometar (20 mg/kg) and immobilized in a dorsal position (Fig. 3). Following scalp removal, pulsed optical illumination (1 mJ pulse energy, 1.4 ns pulse duration, 2 kHz repetition rate, 5 mJ/cm^2 fluence on the skull) was deliverd to the mouse head from a Wedge HB 532-nm (BrightSolutions, Italy) laser using a fibre bundle arrangement [27]. Detection of the OA responses was performed by a home-made PVDF ultrasonic detector ($F = 7.6$ mm focal distance, 0.6 numerical aperture, $A = 9.1$ mm aperture and 5-35 MHz detection band). Reflection-mode OA angiography of the mouse head (7.5×7.5 mm^2 field of view) was performed with 25 μm lateral scanning steps provided by two computer-driven stages M-664 (PI, Germany). Optically-generated probing acoustic pulses excited in the PVDF detector due to the absorption of backscattered laser radiation were utilized for complementary ultrasonic imaging of the same 7.5×7.5 mm^2 area [28].

Biomedical Optics EXPRESS

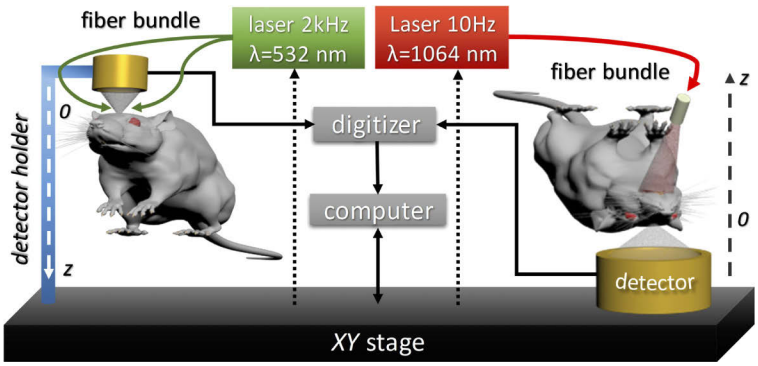

Fig. 3. Schematics of the raster-scan experimental setup employed for *in vivo* OA angiography.

To perform cerebral OA angiography at the wavelength of 1064 nm, a four-week-old nu/nu mouse and 3-day-old rat with intact skull and scalp were used (Fig. 3). The animals were anaesthetized in the same way and immobilized in a ventral position. Stationary pulsed optical illumination (18 ns pulse duration, 10 Hz repetition rate) of the brain at 1064 nm with 100 mJ/cm^2 fluence rate was performed by LS-2137 (LOTIS-TII, Belarus) laser through 50 mm^2 total core area of a fiber bundle (CeramOptec, Germany) consisting of 16 output fiber probes coupled to the lower jaw area of the mouse through an ultrasound gel layer. Transmission-mode ultrasonic detection within the area of 10×10 mm^2 was provided by custom-made PVDF detector ($F = 15$ mm focal distance, 0.77 numerical aperture, $A = 23.1$ mm aperture and 0.2-15 MHz detection band) guided by the same stages M-664 (PI, Germany) with 100 μm lateral scanning steps.

After digitization of the recorded OA data with 200 MHz 16-bit digitizer CSE1622 (GaGe, USA), two post-acquisition algorithms were implemented to improve the resulting OA angiography images. At first, back-projection-based optoacoustic reconstruction algorithm [29] was applied to each *XZ* and *YZ* B-scan. After reconstruction, the volumetric OA image stack was cropped within the depth ranges between z_0=0 mm and z_3=0.7 mm for the 532 nm data and z_0=0 mm and z_3=7 mm for the 1064 nm data ($z_0 = 0$ corresponds to the brain surface) The images at 1064 nm were then processed by Frangi filter [30] to enhance contrast from vessel-like structures at 10-75 μm spatial scales with 10 μm increment. For planar representation of the volumetric datasets, maximum intensity projections (MIP) to *XY* plane with color-encoded depth were applied to the 3D data.

All the *in vivo* experiments were conducted in accordance with international rules of legal and ethical use of animals (NIH Publications No. 8023, revised, 1978). The average radiant exposures at the animal surfaces were compliant with the ANSI Z136.1 standard for laser safety [18].

3. Results and discussion

We calculated the dependence of the integrated optoacoustic pressure upon diameter d and depth D of the blood vessel based on Eq. (4). In order to show the optimal probing laser wavelengths for a given set of parameters, a parametric map of spectral ranges $\lambda(D, d)$ corresponding to $\max_\lambda P(\lambda, D, d)$ was then plotted (Fig. 4(a)). Three characteristic spectral ranges around $\lambda_1 = 580$ nm, $\lambda_2 = 895$ nm, and $\lambda_3 = 1100$ nm were revealed. The existence of three distinct spectral ranges is ascribed to two competing physical phenomena, namely, (1) Stronger absorption by blood leads to stronger OA signals; (2) Stronger light attenuation in the brain leads to limited

Biomedical Optics EXPRESS

penetration depth of the probing optical radiation and diminished OA signals. Thus, for superficial depths where light attenuation is weak the optimal probing wavelength would correspond to the maximum of the blood absorption spectra, i.e. $\lambda_1 = 580$ nm. For greater depths and comparatively thick blood layers ($d > 0.2$ mm) a transition region exists around $\lambda_2 = 895$ nm corresponding to the local minimum of optical absorption in the brain. For deeper locations ($D > 1.5$ mm) attenuation of the probing radiation is the major phenomenon governing the strength of the generated OA signals, thus the optimal wavelength corresponds to the global minimum of the brain absorption spectrum in the range of $\lambda_3 = 1100$ nm.

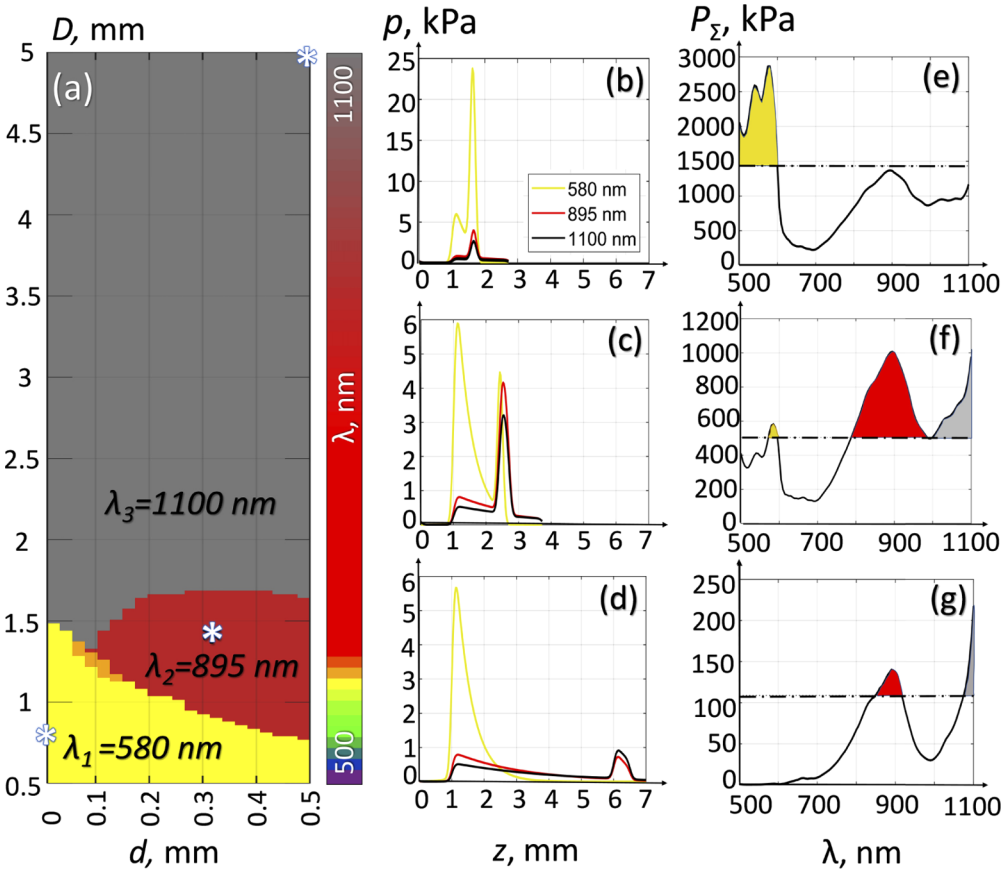

Fig. 4. Optimization of optical wavelengths for cerebrovascular OA imaging: (a) Parametric map of optimal spectral regions for different d and D. The generated OA pressure distribution along the depth axis is depicted in (b), (c) and (d) for $[D, d] = [0.6, 0.1]$, $[1.4, 0.3]$ and $[5, 0.5]$, respectively (also labeled by asterisks in panel a). Wavelength dependence of the cumulative OA contrast factor P_Σ for different vessel depths of $D = 0.6$, 1.4 and 5 mm is plotted in (e), (f) and (g), respectively.

Figure 4(b-d) further depicts the generated OA pressure distribution along the depth axis calculated via Eq. (3) for the wavelengths of $\lambda_1 = 580$ nm, $\lambda_2 = 895$ nm, and $\lambda_3 = 1100$ nm and different pairs of $[D, d] = ([0.6, 0.1], [1.4, 0.3], [5, 0.5])$, as labeled by asterisks in Fig. 4(a). For blood vessels close to the surface (Fig. 4(b)) the maximum OA signal will be generated in the visible spectrum range $\lambda_1 = 580$ nm (Fig. 4(b)). As the depth D of the blood vessel increases (Fig. 4(c)), absorption by the brain layer becomes more pronounced with the magnitude of OA signal from the blood layer becoming comparable to the signal generated at the tissue boundary.

Biomedical Optics EXPRESS

That is why the intermediate spectral range a $\lambda_2 = 895$ nm turns optimal for a certain imaging depth. Obviously, for deeper locations beyond $D = 5$ mm the visible radiation is completely absorbed by the superficial brain layers thus resulting in the negligible OA signals from the deep-seated vessels. When the light attenuation by the brain layer dominates in the OA signal generation process, the optimal wavelength range shifts into the longer wavelength range around 1100 nm where the global minimum of blood absorption occurs. Note, that the value of OA signal from blood layer at $\lambda_3 = 1100$ nm exceeds that for the transition wavelength $\lambda_2 = 895$ nm only slightly, thus the wavelength range of $\lambda_2 = 895$ nm may also be considered for whole-brain OA angiography.

In order to obtain a more general estimate on the wavelength selection independent from the blood vessel size we further defined a cumulative OA contrast factor $P_\Sigma(\lambda, D)$ defined as:

$$P_\Sigma(\lambda, D) = \int_{d_{\min}}^{d_{\max}} P(\lambda, D, x)dx \tag{6}$$

where $[d_{\min},\ d_{\max}] = [0.1\text{ mm},\ 0.5\text{ mm}]$ correspond to the typical size range of cerebral blood vessels in mice. The wavelength-dependence of $P_\Sigma(\lambda, D)$ is plotted in Figs. 4e-g for three representative depths of $D = 0.6$, 1.4, and 5 mm. We then define the threshold for particular wavelength to be optimal for OA angiography as

$$P_\Sigma(\lambda, D) > 0.5 \max_\lambda P_\Sigma(\lambda, D), \tag{7}$$

and represent the threshold level of $0.5 \max_\lambda P_\Sigma(\lambda, D)$ by a horizontal dash-dotted lines in the plots. The optimal wavelength ranges for OA angiography are $\Delta\lambda_1 = [500,600]$ nm, $\Delta\lambda_2 = [570,595] \cup [790,895] \cup [1000,1100]$ nm, $\Delta\lambda_3 = [850,920] \cup [1075,1100]$ nm for the vessel depths of $D = 0.6$, 1.4, and 5 mm, respectively.

Next, we adopted segmented vasculature data from a high resolution μCT scan [21] (Fig. 5(a)) in order to illustrate the expected outcome when employing the determined optimal wavelengths in OA angiography. In particular, we simulated OA images of two vessel plexuses located within brain tissue at depths of 1.0 and 4.1 mm with vessel sizes of 0.2 mm (Fig. 5(b)). The simulations were performed for the three considered wavelengths and two levels of NEP corresponding to the most [2] and the least [31] sensitive PVDF detectors developed by our group. In a simulated image each A-scan was calculated in accordance with Eq. (3) with adding the noise described by the corresponding NEP value. Since 1D model was employed for simulations, no reconstruction procedure was applied. The simulation results (Fig. 5(c)-(g)) confirm that all the considered wavelengths are feasible for OA imaging of the superficial vasculature at depth up to 1 mm, while the deeper located plexus can only be visualized at λ_2 and λ_3 belonging to the optical transparency windows with less significant light attenuation in the brain.

The numerical simulation results are in correspondence with the *in vivo* measurements presented in Fig. 6–7. Figure 6 demonstrates the opportunities of whole-brain in vivo OA angiography of intact newborn rat at 1064 nm in transmission mode. While raw data (Fig. 6(a)) shows only superficial blood vessels (sagittal and transverse sinuses), reconstruction algorithm (Fig. 6(b)) reveals deep structure of cerebral circulatory system. Frangi-filtration allows to enhance the vessels contrast against the background signal originating from bulk tissues and vessel net beyond the resolution limit. Color-encoding of the filtered image (Fig. 6(d)) allows to estimate 3D positions of major blood vessels located at up to 5.5 mm depth. It is worth mentioning, that whole brain OA angiography in this case was obtained owing to small (approximately 0.1 mm) thickness of the newborn rat's skull, while OA imaging through adult rodent's skull and scalp is more challenging.

Traditionally, whole-brain OA angiography of adult rodents is performed after scalp and/or skull removal. Scalp removal allows to overcome multiple scattering barrier for probing optical radiation (see photography of adult mouse head with scalp removed in Fig. 7(a)), however skull

Biomedical Optics EXPRESS

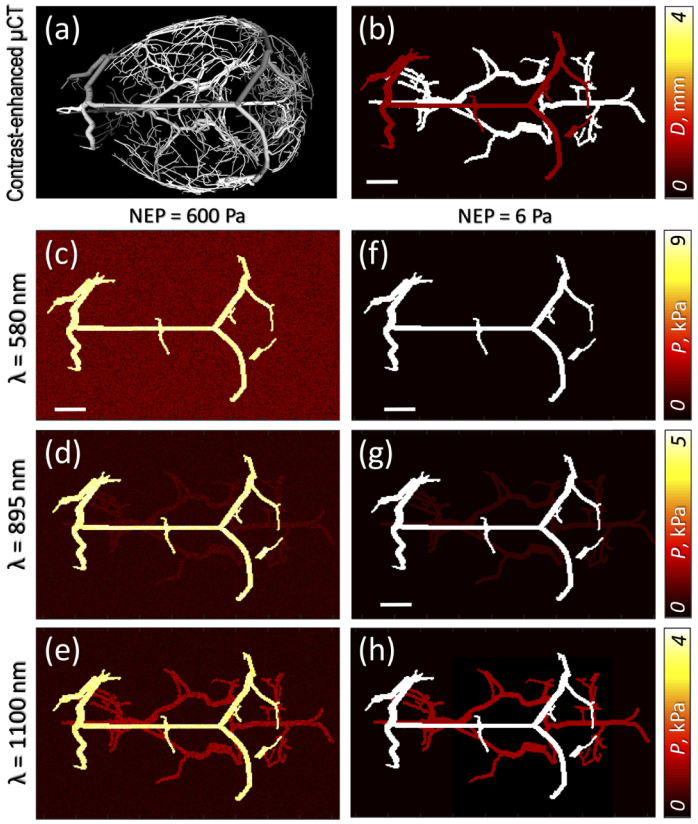

Fig. 5. Numerical simulation of OA imaging of murine cerebral vasculature. (a) Segmented vasculature from contrast-enhanced μCT angiography [32]. (b) Vascular network consisting of two plexuses that was employed for simulations. (c-h) Simulated OA images corresponding to the laser wavelengths of 580 nm (c,f), 895 nm (d,g) and 1100 nm (e,h) and different ultrasound detector sensitivities (maximal intensity projections are shown).

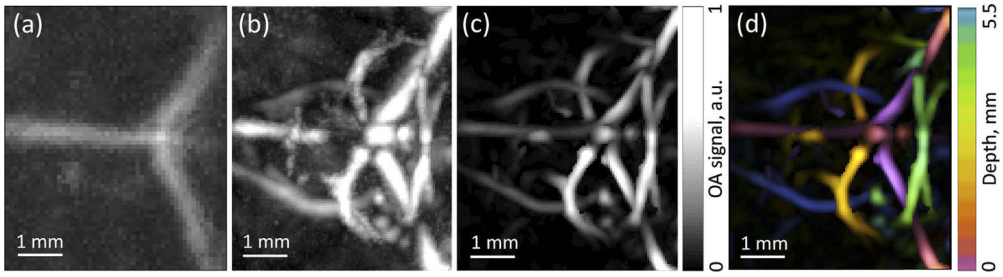

Fig. 6. Whole-brain in vivo OA angiography of intact newborn rat at 1064 nm in transmission mode: raw OA image (a), OA image after reconstruction (b), and conventional (c) and depth-encoded (d) OA images after reconstruction and Frangi-filtration. The images represent maximal intensity projections along the depth axis.

Biomedical Optics EXPRESS

is a barrier for ultrasound signal (note the skull contrast in ultrasound image of adult mouse head in Fig. 7(b)). Higher-frequency acoustic detector employed for OA angiography at 532 nm laser wavelength in reflection geometry allowed to overcome these limitations and revealed fine structure of cerebral circulatory system in the depth range of 0-0.7 mm (Fig. 7(c)).

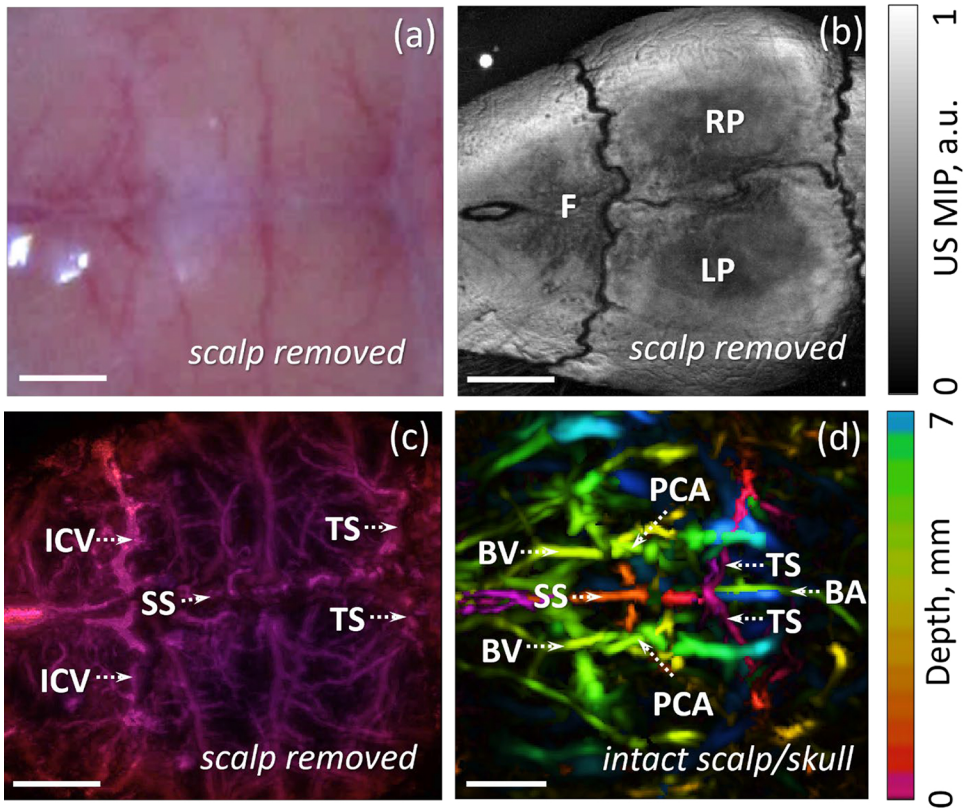

Fig. 7. In vivo images of the mouse brain through removed or intact scalp. (a) Photography of the scanning region. (b) Laser-ultrasound image of the skull taken at 532 nm in reflection mode. (c) OA image taken at 532 nm in reflection mode. (d) Whole-brain OA angiography at 1064 nm in transmission mode through intact skin and skull. Scale bar - 1 mm. F – frontal bone, RP – right parietal bone, LP – left parietal bone, BV-basal vein, SS-sagittal sinus, PCA - posterior communicating artery, TS - transverse sinus, ICV- inferior cerebral vein; BA - basilar artery.

For longer depth range (0-7 mm) transillumination mode at 1064 nm laser wavelength together with low-frequency acoustic detection was employed allowing for mapping major blood vessels in intact adult mouse (Fig. 7(d)). As a result, all the major blood vessels were attributed in accordance with the brain atlas (Fig.5a): while the sagittal (SS) and transverse (TS) sinuses were located on the dorsal side of the brain dura mater at the depths $D < 1$ mm, the basilar (BA) and posterior communicating (PCA) arteries, as well as the basal vein (BV) were located in the ventral side of the rodent brain at 5-6 mm depth.

4. Conclusion

In this manuscript we report on a comprehensive theoretical analysis of the optimal wavelengths for in vivo OA angiography in whole rodent brains. Governed by the competing processes of light attenuation through the brain tissues and OA signal generation due to absorption by blood,

Biomedical Optics EXPRESS

we identified three distinct spectral ranges centered around 580, 895 and 1100 nm optimally suited for imaging of vessels of different size and depth. The developed model was employed for numerical simulation of OA imaging of murine brain illustrating the effect of probing wavelength on visibility of the cerebral vasculature. In vivo imaging experiments further affirmed the capacity for whole-brain OA angiography in rodents at a wavelength of 1064 nm.

Appendix

We consider one-dimensional propagation of the incident probing laser pulse of a unit energy inside a semi-infinite layer of soft brain tissue covered by skull. After passing through a highly diffusive layers of scalp and skull of the thicknesses η and ξ, respectively, the distribution of light illuminating the brain can be assumed close to isotropic and the energy loss in the scalp and skull can be take into account by the factor $\exp(-(\langle\mu_{t,scalp}\rangle\eta + \langle\mu_{t,s}\rangle\xi))$ in accordance with the Delta-Eddington approximation [17].

The in-depth dependence of the probing energy in brain can be derived by integrating the well-known dipole solution of the 3D diffusion equation for the unit point source at the boundary of the refractive index-matched semi-infinite layer [21]:

$$P_{3D}(r,z) = \frac{3\mu_{t,B}}{4\pi}\left(\frac{\exp(-\mu_B R_1)}{R_1} - \frac{\exp(-\mu_B R_2)}{R_2}\right), \tag{8}$$

where $R_{1,2} = \sqrt{(\boldsymbol{r}-\boldsymbol{r}_0)^2 + (z-z_{1,2})^2}$, $\boldsymbol{r}$ and z are, correspondingly, the lateral and axial position of the observation point with respect to the origin, $z_1 = 0$ and, $z_2 = -2/(3\mu_{t,B})$ is the position of the extrapolated boundary. We neglect refractive index mismatch between the layers of the rodent head assuming the effects of refraction are inconsiderable for the water-scalp and skull-brain interfaces. By surface integration of Eq. (A1) over all possible lateral positions r_0 of the isotropic source we obtain:

$$P_{1D}(z) = \frac{3\mu_{t,B}}{2\mu_B}(\exp(-\mu_B z) - \exp(-\mu_B(z + 2/(3\mu_{t,B})))). \tag{9}$$

The energy in-depth profile in the brain is then calculated as follows:

$$P_B(z) = \frac{3\mu_{t,B}}{\mu_B}\exp(-(\langle\mu_{t,scalp}\rangle\eta + \langle\mu_{t,s}\rangle\xi))\exp\left(-\frac{\mu_B}{3\mu_{t,B}}\right)\sinh\left(\frac{\mu_B}{3\mu_{t,B}}\right)\exp(-\mu_B z) = k_B\exp(-\mu_B z),$$

where

$$k_B = \frac{3\mu_{t,B}}{\mu_B}\exp\left(-\frac{\mu_B}{3\mu_{t,B}}\right)\sinh\left(\frac{\mu_B}{3\mu_{t,B}}\right)\exp(-(\langle\mu_{t,scalp}\rangle\eta + \langle\mu_{t,s}\rangle\xi)).$$

Funding

Russian Science Foundation (18-45-06006); Helmholtz Association (HRSF-0020).

Acknowledgement

The authors are grateful to Maxim Prudnikov, Roman Belyaev and Vladimir Vorobyev for their engineering contributions to this work, to Dr. Michael Jaeger for providing the reconstruction algorithm, and to Dr. James Guggenheim for experimental estimations of NEP of PVDF detector.

Disclosures

The authors declare that there are no conflicts of interest related to this article.

Biomedical Optics EXPRESS

References

1. L. V. Wang and S. Hu, "Photoacoustic tomography: in vivo imaging from organelles to organs," Science **335**(6075), 1458–1462 (2012).
2. P. Subochev, A. Orlova, E. Smolina, A. Kirillov, N. Shakhova, and I. Turchin, "Raster-scan optoacoustic angiography reveals 3D microcirculatory changes during cuffed occlusion," Laser Phys. Lett. **15**(4), 045602 (2018).
3. M. Toi, Y. Asao, Y. Matsumoto, H. Sekiguchi, A. Yoshikawa, M. Takada, M. Kataoka, T. Endo, N. Kawaguchi-Sakita, and M. Kawashima, "Visualization of tumor-related blood vessels in human breast by photoacoustic imaging system with a hemispherical detector array," Sci. Rep. **7**(1), 41970 (2017).
4. A. Karlas, N.-A. Fasoula, K. Paul-Yuan, J. Reber, M. Kallmayer, D. Bozhko, M. Seeger, H.-H. Eckstein, M. Wildgruber, and V. Ntziachristos, "Cardiovascular optoacoustics: From mice to men–A review," J. Photoacoust. **14**, 19–30 (2019).
5. S. V. Ovsepian, I. Olefir, G. Westmeyer, D. Razansky, and V. Ntziachristos, "Pushing the boundaries of neuroimaging with optoacoustics," Neuron **96**(5), 966–988 (2017).
6. X. Wang, Y. Pang, G. Ku, G. Stoica, and L. V. Wang, "Three-dimensional laser-induced photoacoustic tomography of mouse brain with the skin and skull intact," Opt. Lett. **28**(19), 1739–1741 (2003).
7. J. Yao, L. Wang, J.-M. Yang, K. I. Maslov, T. T. Wong, L. Li, C.-H. Huang, J. Zou, and L. V. Wang, "High-speed label-free functional photoacoustic microscopy of mouse brain in action," Nat. Methods **12**(5), 407–410 (2015).
8. J. Rebling, H. Estrada, S. Gottschalk, G. Sela, M. Zwack, G. Wissmeyer, V. Ntziachristos, and D. Razansky, "Dual-wavelength hybrid optoacoustic-ultrasound biomicroscopy for functional imaging of large-scale cerebral vascular networks," J. Biophotonics **11**(9), e201800057 (2018).
9. P. Zhang, L. Li, L. Lin, P. Hu, J. Shi, Y. He, L. Zhu, Y. Zhou, and L. V. Wang, "High-resolution deep functional imaging of the whole mouse brain by photoacoustic computed tomography in vivo," J. Biophotonics **11**(1), e201700024 (2018).
10. S. Gottschalk, O. Degtyaruk, B. Mc Larney, J. Rebling, M. A. Hutter, X. L. Deán-Ben, S. Shoham, and D. Razansky, "Rapid volumetric optoacoustic imaging of neural dynamics across the mouse brain," Nat. Biomed. Eng. **3**(5), 392–401 (2019).
11. P. K. Upputuri and M. Pramanik, "Photoacoustic imaging in the second near-infrared window: a review," J. Biomed. Opt. **24**(04), 1 (2019).
12. Z. Sheng, B. Guo, D. Hu, S. Xu, W. Wu, W. H. Liew, K. Yao, J. Jiang, C. Liu, and H. Zheng, "Bright Aggregation-Induced-Emission Dots for Targeted Synergetic NIR-II Fluorescence and NIR-I Photoacoustic Imaging of Orthotopic Brain Tumors," Adv. Mater. **30**(29), 1800766 (2018).
13. A. Orlova, A. Maslennikova, G. Y. Golubiatnikov, A. Suryakova, M. Y. Kirillin, D. Kurakina, T. Kalganova, A. Volovetsky, and I. Turchin, "Diffuse optical spectroscopy assessment of rodent tumor model oxygen state after single-dose irradiation," Biomed. Phys. Eng. Express **5**(3), 035010 (2019).
14. N. Bosschaart, G. J. Edelman, M. C. Aalders, T. G. van Leeuwen, and D. J. Faber, "A literature review and novel theoretical approach on the optical properties of whole blood," Lasers Med. Sci. **29**(2), 453–479 (2014).
15. P. Van der Zee, "Measurement and modelling of the optical properties of human tissue in the near infrared," (1992).
16. A. Sarvazyan and C. Hill, "Physical chemistry of the ultrasound-tissue interaction," *Physical Principles of Medical Ultrasonics* **7**, 223–235 (2004).
17. B. T. Cox, J. G. Laufer, P. C. Beard, and S. R. Arridge, "Quantitative spectroscopic photoacoustic imaging: a review," J. Biomed. Opt. **17**(6), 061202 (2012).
18. A. N. S. Institute, *American national standard for safe use of lasers* (Laser Institute of America, 2007).
19. H. Soleimanzad, H. Gurden, and F. Pain, "Optical properties of mice skull bone in the 455-to 705-nm range," J. Biomed. Opt. **22**(1), 010503 (2017).
20. C. P. Sabino, A. M. Deana, T. M. Yoshimura, D. F. da Silva, C. M. França, M. R. Hamblin, and M. S. Ribeiro, "The optical properties of mouse skin in the visible and near infrared spectral regions," J. Photochem. Photobiol., B **160**, 72–78 (2016).
21. T. J. Farrell, M. S. Patterson, and B. Wilson, "A diffusion theory model of spatially resolved, steady-state diffuse reflectance for the noninvasive determination of tissue optical properties in vivo," Med. Phys. **19**(4), 879–888 (1992).
22. R. C. Haskell, L. O. Svaasand, T.-T. Tsay, T.-C. Feng, M. S. McAdams, and B. J. Tromberg, "Boundary conditions for the diffusion equation in radiative transfer," J. Opt. Soc. Am. A **11**(10), 2727–2741 (1994).
23. S. L. Jacques, "How tissue optics affect dosimetry of photodynamic therapy," J. Biomed. Opt. **15**(5), 051608 (2010).
24. M. Kneipp, J. Turner, H. Estrada, J. Rebling, S. Shoham, and D. Razansky, "Effects of the murine skull in optoacoustic brain microscopy," J. Biophotonics **9**(1-2), 117–123 (2016).
25. H. Estrada, J. Rebling, and D. Razansky, "Prediction and near-field observation of skull-guided acoustic waves," Phys. Med. Biol. **62**(12), 4728–4740 (2017).
26. J. A. Guggenheim, J. Li, T. J. Allen, R. J. Colchester, S. Noimark, O. Ogunlade, I. P. Parkin, I. Papakonstantinou, A. E. Desjardins, and E. Z. Zhang, "Ultrasensitive plano-concave optical microresonators for ultrasound sensing," Nat. Photonics **11**(11), 714–719 (2017).
27. A. Orlova, M. Sirotkina, E. Smolina, V. Elagin, A. Kovalchuk, I. Turchin, and P. Subochev, "Raster-scan optoacoustic angiography of blood vessel development in colon cancer models," J. Photoacoust. **13**, 25–32 (2019).
28. P. Subochev, A. Orlova, I. Mikhailova, N. Shilyagina, and I. Turchin, "Simultaneous in vivo imaging of diffuse optical reflectance, optoacoustic pressure, and ultrasonic scattering," Biomed. Opt. Express **7**(10), 3951–3957 (2016).

Biomedical Optics EXPRESS

29. M. Jaeger, S. Schüpbach, A. Gertsch, M. Kitz, and M. Frenz, "Fourier reconstruction in optoacoustic imaging using truncated regularized inverse k-space interpolation," Inverse Problems **23**(6), S51–S63 (2007).
30. T. Oruganti, J. G. Laufer, and B. E. Treeby, "Vessel filtering of photoacoustic images," Proc. SPIE **8581**, 85811W (2013).
31. P. V. Subochev, M. Prudnikov, V. Vorobyev, A. S. Postnikova, E. Sergeev, V. V. Perekatova, A. G. Orlova, V. Kotomina, and I. V. Turchin, "Wideband linear detector arrays for optoacoustic imaging based on polyvinylidene difluoride films," J. Biomed. Opt. **23**(09), 1 (2018).
32. S. Ghanavati, J. P. Lerch, and J. G. Sled, "Automatic anatomical labeling of the complete cerebral vasculature in mouse models," NeuroImage **95**, 117–128 (2014).